RSC Advances

PAPER

View Article Online
View Journal | View Issue

Cite this: *RSC Adv.*, 2026, **16**, 14420

Upcycling boiler fuel rice-husk waste: a sustainable cellulose–clay nanocomposite for lead remediation

Mirza Nusrat Sweety,[a] Shamima Akther Eti,*[ab] Muhammad Amirul Hoque,[a] Mohammad Shahid Ullah,[c] Shabiba Parvin Shandhi,[a] Fariha Chowdhury,[d] Md. Khabir Uddin Sarker,[a] Sarna Khanam,[a] Farid Ahmed[e] and Mohammad Mahbubur Rahman *[a]

A novel approach for the utilization of a boiler fuel rice-husk silica waste-based cellulose–clay nanocomposite (CCN) has been developed for the first time, and it has been assessed as a green adsorbent for the removal of Pb^{2+} from water. The addition of cellulose, which is rich in hydroxyl groups, along with the layered clay, enhanced the surface reactivity, porosity, and structural stability of the resulting composite. The CCN was characterized through a variety of methods, including Fourier transform infrared spectroscopy (FT-IR), X-ray diffraction (XRD), thermogravimetric analysis (TGA), scanning electron microscopy with energy dispersive X-ray spectroscopy (SEM-EDX), Zetasizer, and UV-vis spectroscopy. Characterization of the CCN confirmed the development of a well-integrated composite featuring numerous active sites. A specially designed dynamic packed column adsorption system showed quick and efficient uptake of Pb^{2+}, where the removal effectiveness of the CCN was influenced by several factors such as pH, initial concentration, and contact time. The CCN achieved an impressive adsorption capacity of 195.80 mg g^{-1} under controlled flow rates, adsorption dosage, and pH conditions. These findings underscore the potential of CCNs as affordable and high-performance materials for the remediation of heavy metals in wastewater treatment.

Received 5th February 2026
Accepted 11th March 2026

DOI: 10.1039/d6ra01013j

rsc.li/rsc-advances

1. Introduction

For both developed and developing nations, chemical pollution—particularly that caused by heavy metals—is the aspect of the water pollution issue that receives the most attention.[1] Because of contaminants' detrimental effects on ecosystems and human health, heavy metal contamination is a serious environmental concern. Industrial processes like battery manufacturing, mining, and smelting, as well as inappropriate disposal of electronic waste, can introduce Pb, a common heavy metal, into water systems.[2,3] The harmful effects of Pb pollution on the environment and human health have made it a growing concern in water bodies.[4] Especially among children, lead poisoning can cause serious health problems like kidney damage, neurotoxicity, and developmental disorders.[5,6] Consequently, it is crucial to remove lead from aqueous systems.

Innumerable validated methods are available for eliminating wastewater contaminants, among which adsorption has become widely recognized as one of the most effective technologies for the removal and potential recovery of heavy metals from aqueous solution.[7,8] Nonetheless, in an adsorption process, appropriate choice of adsorbent is essential. Because of the high surface area, chemical versatility, and biodegradability, clay and cellulose—two naturally occurring materials—have been used as adsorbents in both unmodified and modified forms. They have also drawn a lot of interest as adsorbent base materials.[9–11] Because cellulose contains –OH groups, which give it exceptional reactivity, this biopolymer can be used either alone or in composites with other materials, like clay, to treat water.[12] Several studies are found showing that, due to its distinct characteristics, including strong mechanical strength, resistance to chemicals, biodegradability, and numerous possible chemical modifications, different form of cellulose such as: polyvinyl alcohol/carboxymethyl cellulose/ZSM-5 zeolite biocomposite membranes,[13] PVA/CMC/halloysite nanoclay bio composite,[14] and ZSM-5 zeolite/polyvinyl alcohol/carboxymethyl cellulose/sodium alginate bio composite[15] *etc.*

[a]*Fiber and Polymer Research Division, BCSIR Dhaka Laboratories, Bangladesh Council of Scientific and Industrial Research, Dhaka-1205, Bangladesh. E-mail: mahbub.bcsir@yahoo.com; Shaeti123@gmail.com*

[b]*School of Natural Sciences, Institute of Physics, University of Galway, Ireland*

[c]*Department of Arts and Sciences, Faculty of Engineering, Ahsanullah University of Science and Technology (AUST), 141-142, Love Road, Tejgaon I/A, Dhaka-1208, Bangladesh*

[d]*Biomedical and Toxicology Research Institute, Bangladesh Council of Scientific and Industrial Research, Dhaka-1205, Bangladesh*

[e]*Institute of Glass and Ceramic Research and Testing, Bangladesh Council of Scientific and Industrial Research, Dhaka-1205, Bangladesh*

have been utilized as an adsorbent in various wastewater treatment systems. However, octahedral aluminates, hydrated tetrahedral silicates, and crystals of other minerals with high surface area and complex porous structure make up the majority of the chemical structure of clay minerals, despite the fact that they exist in a variety of physical forms.[16,17] Because of their high cation exchange capacities, surface reactivity, and availability, clay minerals like kaolinite and montmorillonite are perfect for heavy metal adsorption.[18] By combining the advantages of both materials, cellulose and clay can be combined to create a nanocomposite that offers improved adsorption efficiency through synergistic effects like increased surface area, availability of functional groups, and structural stability.[19] The adsorption capacities of composite materials are richer than those of the individual composite members.

Therefore, by taking advantage of their distinct physico-chemical characteristics, the clay and cellulose composite may have a great deal of promise for the effective removal of extremely hazardous heavy metals like lead Pb^{2+}. Sodium montmorillonite (NaMMT) can also be used to modify cellulose for use as an adsorbent. Cellulose montmorillonite, a composite biomaterial, is the altered product. Cr(VI) can be eliminated from aqueous solutions using it. Large-scale water treatment applications can benefit from these composites' low synthesis costs, environmental friendliness, and reusability.[20] However, variables like type of clay, modification of cellulose, and operating conditions affect how well these composites perform.[21–24]

This study aims at the development and characterization of a novel cellulose–clay nanocomposite (CCNs) for the effective removal of Pb^{2+} ions from aqueous solutions. To date, numerous studies exist on cellulose–clay composites or biocomposites for various applications, demonstrating the utilization of available clay sources as raw materials.[7,20,28] In our study, the clay was sourced from boiler fuel rice-husk silica waste and utilized post-modification with surfactant (MTABr), which enhances the significance of this research. In this study, the waste from rice husk silica is transformed into a valuable product that is suitable for environmental heavy metal (Pb^{2+}) remediation. The method of clay preparation from boiler fuel rice-husk silica waste has not been investigated for developing nanocomposites with cellulose. Following the CCNs' preparation, various analytical techniques such as FTIR, SEM-EDX, XRD, UV-vis, DLS, and TGA validated the formation of CCNs. Subsequently, a filled column was constructed utilizing layers of prepped adsorbents along with supplementary support materials (such as sand, synthetic fibers, *etc.*) to evaluate the efficiency of CCNs in removing Pb^{2+} metal ions from water. The influence of several factors on the adsorption capacity of CCNs was analyzed, such as pH, dosage, contact duration, and initial lead concentration. Finally, different isotherms (Langmuir, Freundlich, and Temkin) and kinetic models (pseudo-first-order, pseudo-second-order, and intra-particle diffusion) were employed to confirm the adsorption mechanisms. The findings of this research will assist in creating a sustainable, cost-effective, and eco-friendly nano-composite for purifying wastewater.

2. Materials and methods

2.1 Materials

Commercially available cellulose powder (CAS 9004-34-6, white color, grain size for column chromatography, fiber size 0.01–0.1 mm) from Merck KGaA, Germany, was used as the primary biopolymer, and myristyl trimethyl ammonium bromide (MTABr) (Sigma-Aldrich, Germany, purity: ≥99%) was used for the synthesis of the composite. Boiler furnace ash collected from the Dinajpur rice mill was used as a raw material for clay. Analytical grade acetone (Sigma-Aldrich, Germany) was used for the dispersion of clay. Lead(II) acetate $Pb(C_2H_3O_2)_2 \cdot 3H_2O$ (≥99.99% trace metals basis, CAS 6080-56-4, Sigma-Aldrich) solution as the lead ions source was used for the adsorption experiments. Hydrochloric acid (Merck, Germany, purity: 98%) and sodium hydroxide (Merck, Germany, purity: 98%) were used for pH stabilization, and deionized water was used for solution preparation.

2.2 Methods

2.2.1 Preparation of the clay. Boiler fuel rice-husk silica treated with deionized water and HCl was dried at 80 °C overnight. The clay was subsequently ground into a fine powder using a planetary ball mill (Pulverisette 5; Fritsch GmbH) equipped with a 500 mL zirconium dioxide bowl and 80 zirconium dioxide balls (1 cm in diameter). The milling process was conducted at a frequency of 300 rpm for 2 h. The clay powder was then separated into different particle sizes using a mechanical sieve shaker. Particle-size separation was conducted utilizing a vibratory sieve shaker (ANALYSETTE 3 PRO, FRITSCH GmbH, Germany) equipped with stainless-steel test sieves with mesh sizes (500, 250, 125, 75, and 45 μm) organized in descending sequence. 100 g of dried clay powder was sifted for 10 minutes at a regulated vibratory amplitude, yielding various fractions of clay powder based on particle size. The instrument's two-dimensional vibrational movement guaranteed consistent separation of particles throughout the sieve series. A solution of 0.001 mol L^{-1} MTABr was prepared by diluting it with deionized water. 6 g of 125 mesh sizes of the clay were mixed with 20 mL of acetone. To achieve optimal swelling and dispersion of the clay, 100 mL of MTABr solution was introduced into the clay suspension. The suspension was stirred magnetically for 8 h at 800 rpm. The mixture was centrifuged at least three times. The solid material was then washed with water until it became free of bromide. The elimination of bromide was confirmed through the $AgNO_3$ test. The sample was taken in a test tube, and 50 mL of 0.1 M $AgNO_3$ solution was added dropwise. No precipitation confirmed the absence of bromide.[20] The sample was then dried overnight at 80 °C. The overall clay preparation scheme is depicted in Fig. 1.

2.2.2 Preparation of cellulose clay nano-composite (CCNs). A clay suspension was prepared using 6 g, 6.5 g, 7 g, and 7.5 g of clay in 20 mL of acetone. Three grams of cellulose powder were gradually added to the prepared clay suspension and stirred for 12 hours at 60 °C. The resulting adsorbent was rinsed with deionized water and air dried at 105 °C for 6 hours, as is

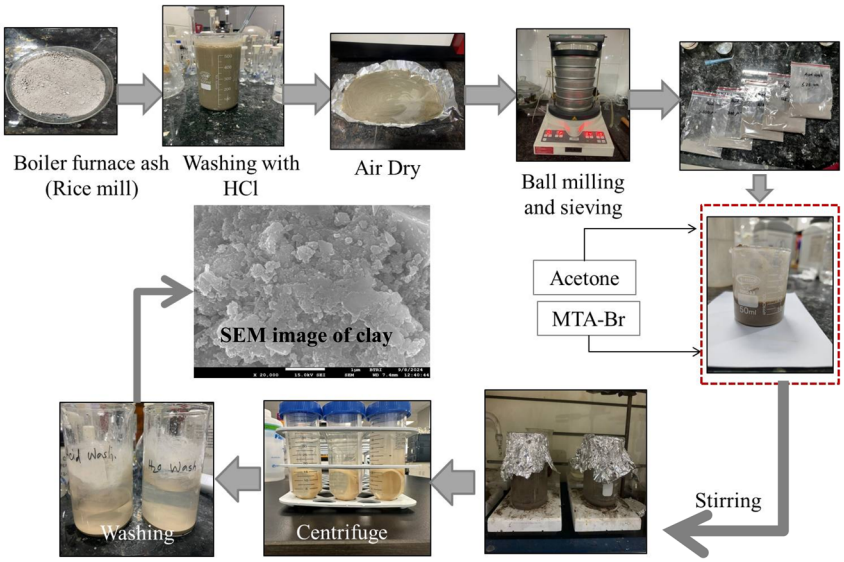

Fig. 1 Preparation of clay.

illustrated in Fig. 2, and was utilized for subsequent studies. 4 batches were prepared and named as CCN-1, CCN-2, CCN-3, and CCN-4 respectively.

2.2.3 Construction of packed column. A 500 mL cylindrical shaped glass column of 32.5 mm radius with solid glass stopcock (G 20 SCHOTTuGEN & MAINZ, 500 mL) was assembled utilizing layers of synthesized CCNs of various weights of (0.05, 0.075, 0.1, 0.125, and 0.15 g) along with 5 g of sand (100 g; lead(II) adsorption capacity, 0.92 mg g^{-1}). To secure the column's stability and guarantee the even distribution of the metal ion solution throughout, layers of 1 g synthetic polypropylene fiber, (1 g, lead(II) adsorption capacity, 2.7 mg g^{-1}) were incorporated at both the bottom and top sections of the column, as is illustrated in Fig. 3. Polypropylene fiber was used due to its durability, low moisture absorption capacity, availability, light weight, and cost effectiveness.[25]

2.3 Characterization of the CCNs

2.3.1 Fourier transform infrared spectroscopy (FTIR). To detect functional groups and validate chemical interactions between cellulose and clay, Fourier transform infrared spectroscopy (Frontier, PerkinElmer, UK) was used. In transmittance mode, 16 scans of the infrared spectra were made for each test, with a wavenumber range of 500–4000 cm^{-1} and a resolution of 4 cm^{-1}.

2.3.2 X-ray diffraction (XRD). To investigate the crystallographic property of the synthesized product, an XRD equipment from Rigaku SmartLab was used. The data were gathered at intervals of 0.01 and 30° min^{-1} scan speed within the 2-theta range of 5–90°. The chiller temperature was kept at 23 °C while data was being collected using a copper X-ray source operating at 40 kV and 50 mA. Before the detector, a Ni filter was positioned to remove the X-ray source's β-rays.

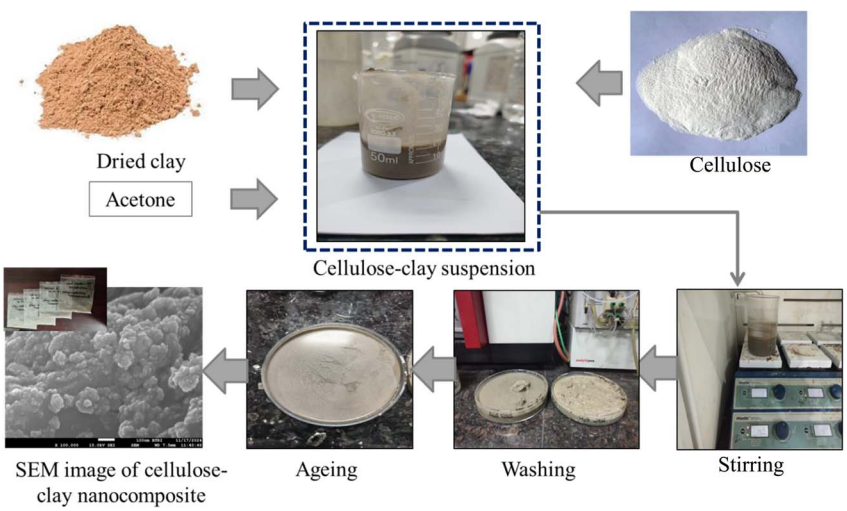

Fig. 2 Preparation of cellulose–clay nano-composite (CCN).

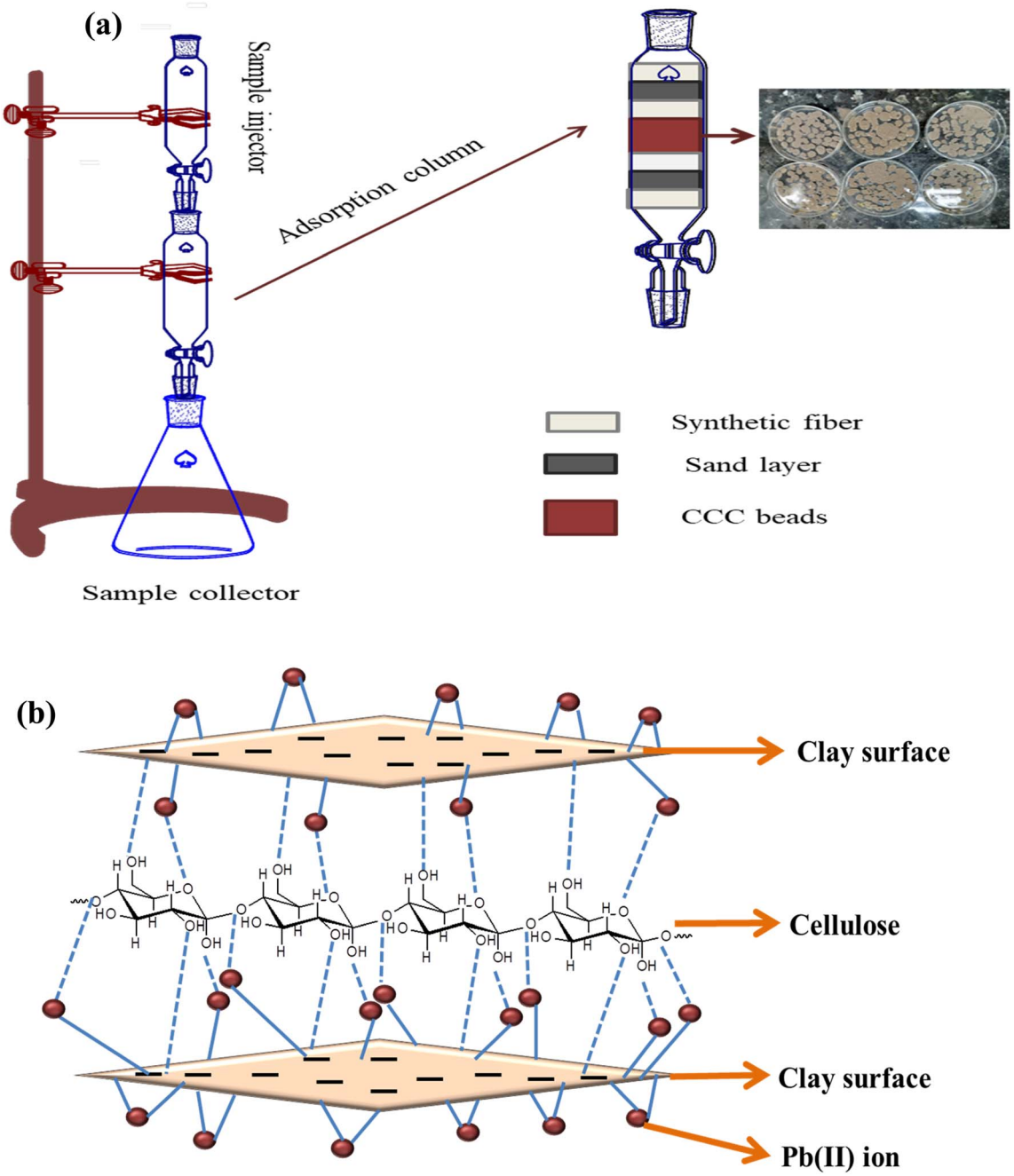

Fig. 3 (a) Set up of the packed column, and (b) mechanism for Pb^{2+} adsorption.

2.3.3 Scanning electron microscopy (SEM). The surface morphology of the prepared sample was studied by FESEM attached with an energy dispersive X-ray spectrometer (JSM-7610F). The voltage applied was 15.00 kV. The samples were measured with different magnifications (100 000, 50 000, 30 000) and different scales (1 μm, 100 nm). EDX analysis was carried out to see the atom% and mass% of the elements present in the samples. Before the analysis, a JEOL (JEC-3000FC) auto fine coater was used to coat the samples. In the JEOL JEC-3000FC Auto Fine Coater, platinum (Pt) is the primary and standard conductive substance used to cover samples for SEM imaging. The particle sizes of the CCNs were calculated by ImageJ software using the SEM images. 25 particles of each sample were measured by the software and the data obtained were further calculated in Origin software to get the average particle size of the CCN.

2.3.4 Zeta potential and hydrodynamic diameter. The colloidal characteristics of the synthesized powder were investigated by the Zetasizer [Zetasizer Ultra, Malvern, UK] utilized for the dynamic light scattering (DLS) technique. Evaluated the stability and hydrodynamic diameter by dispersing the samples in water using an ultrasonic bath [POWERSONIC 510, United Kingdom] at ambient temperature (30 °C) for 60 minutes. The hydrodynamic diameters were calculated using the Stokes–Einstein equation.

2.3.5 Thermogravimetric analysis. The thermal stability of the prepared CCNs was carried out by using a TGA equipment (model: Pyris 1, Brand: PerkinElmer, Origin: Germany). The nitrogen flow rate was maintained at 20 mL min^{-1} while heating at 20 °C min^{-1} to a temperature of 30 to 850 °C. The breakdown of the samples or the temperature withstand ability of the samples was observed from this analysis.

2.3.6 UV-vis analysis. The absorption maxima was studied based on the absorption frequency data obtained from a UV-vis spectrophotometer (Lambda 35, PerkinElmer, Germany) in the wavelength range of 300–700 nm. In this analysis, the CCNs were analyzed directly in solid form at room temperature. From the absorbance data, the band gap was calculated incorporating Tauc plot. From the absorbance maxima and band gap data, composites ability to remove Pb^{2+} was observed.

2.4 Batch adsorption experiments

The adsorption of Pb^{2+} by the synthesized CCN-1 was investigated using batch adsorption experiments. The basic difference between the four batches was the quantity of clay used (6 g, 6.5 g, 7 g, and 7.5 g for CCN-1, CCN-2, CCN-3, and CCN-4, respectively). Among them, CCN-1 exhibited high crystallinity with the smallest and most uniform particle size. The thermal stability, band gap characteristics, and smallest hydrodynamic diameter also rendered CCN-1 more desirable. The reason might be that 6 g of clay works well with 3 g of cellulose to create a composite instead of another composition. Hence, CCN-1 was chosen to execute the batch experiment. To analyze the CCN-1 dosage effect, the adsorbents from 0.05 to 0.15 g were employed for 60 minutes at 30 ± 0.5 °C, and with a Pb^{2+} concentration of 100 mg L^{-1}. To analyze the initial concentration effect, in each experiment, 100 mL of $Pb(NO_3)_2$ solution contained 0.1 g of CCN-1 containing beads at varying concentrations (25–150 mg L^{-1}) for 60 minutes at 30 ± 0.5 °C. The working solution was diluted with either 0.1 M HCl or 0.1 M NaOH to determine the ideal pH for the adsorption experiments. Experiments were carried out in the pH range of 4.0–9.0 in order to investigate the impact of solution pH on the adsorption of metals. The effect of flow rate on the Pb^{2+} adsorption in the packed column was also investigated with flow rate from 1 to 10 mL min^{-1}, the initial Pb^{2+} concentration was kept at 100 mg L^{-1} at pH = 6, and at 30 ± 0.5 °C throughout the experiments. The solution was filtered following adsorption, and Atomic Absorption Spectroscopy (NovAA 400P, Analytik Jena, Germany) was used to measure the remaining Pb^{2+} ion concentration.

2.4.1 Isotherm and kinetic studies. At room temperature, the solution was introduced in a downward flow configuration for the adsorption experiments. An Atomic Absorption Spectrometer (AAS) (NovAA 400P, Analytik Jena, Germany) was used to analyze the filtrate gathered at the packed column's outlet. This study aims to assess the impact of different parameters on Pb^{2+} adsorption, such as the following:

- Contact time at various intervals (ranging from 5 to 180 minutes).
- Initial Pb(II) concentrations of (25–150) mg L^{-1}, with varying contact times (5–180 minutes).
- Initial pH values ranging from 4 to 9 at optimum contact time.
- Adsorbent doses of 0.05, 0.075, 0.1, 0.125, and 0.15 g at the optimum contact time and optimum pH 6.

The adsorption capacity (Q_e), and the removal efficiency (%) were estimated by engaging the following equations:

$$Q_e = (C_i - C_e/M) \times V \quad (1)$$

$$\text{Removal efficiency} = (C_i - C_e/C_i) \times 100 \quad (2)$$

where Q_e stands for the adsorption capacity (mg g^{-1}), V (L) denotes the volume of the solution, M (g) for the mass of the adsorbent, C_i and C_e (mg L^{-1}) represent the initial and final concentrations of Pb(II), respectively.

2.4.1.1 Adsorption kinetics. The adsorption mechanism was studied by engaging different kinetic models, including pseudo-first order, pseudo-second order kinetic model, and intra-particle diffusion model for this adsorption. The following equations are employed to study the models:

Pseudo-first order kinetic model:

$$\ln(Q_e - Q_t) = \ln Q_e - k_1 t \quad (3)$$

Pseudo-second order kinetic model:

$$\frac{t}{Q_t} = 1/k_2 Q_e^2 + t/Q_e \quad (4)$$

Intra-particle diffusion model:

$$Q_t = K_{diff} \times t^{1/2} + C \quad (5)$$

where, Q_e = the adsorption amounts (mg g^{-1}) at equilibrium (min), Q_t = the adsorption amounts (mg g^{-1}) at time t, k_1 (min^{-1}) = the rate constant for the pseudo-first order, k_2 (g mg^{-1} min^{-1}) = the rate constants for the pseudo-second order kinetic adsorption, and K_{diff} (mg (g^{-1} $min^{-1/2}$)) = the rate constant for the intra-particle diffusion, respectively. The letter C denotes the boundary layer's thickness.

2.4.1.2 Adsorption isotherm. A total of three isotherm models were incorporated to analyze the resulting data in order to characterize the interaction between Pb^{2+} and the composite adsorbent and assess the equilibrium adsorption properties. The linear forms of these adsorption isotherms utilized in the investigation are listed below:

Langmuir isotherm model equation:

$$C_e Q_e = 1/Q_m K_L + C_e Q_m \quad (6)$$

Freundlich isotherm model equation:

$$\ln Q_e = \ln K_F + \frac{1}{n} \ln C_e \quad (7)$$

Temkin isotherm model equation:

$$Q_e = B \ln K_T + B \ln C_e \quad (8)$$

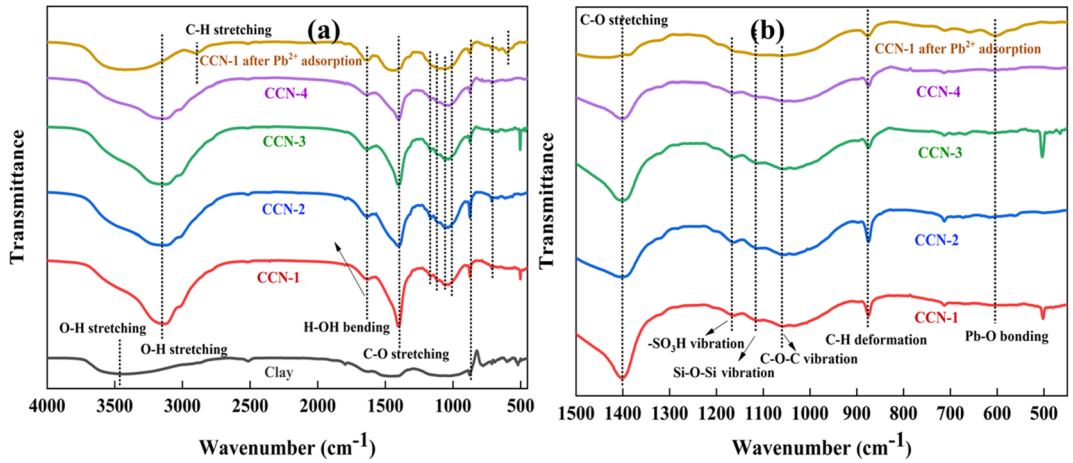

Fig. 4 (a and b) FTIR spectra of clay, prepared CCNs before and after Pb^{2+} adsorption.

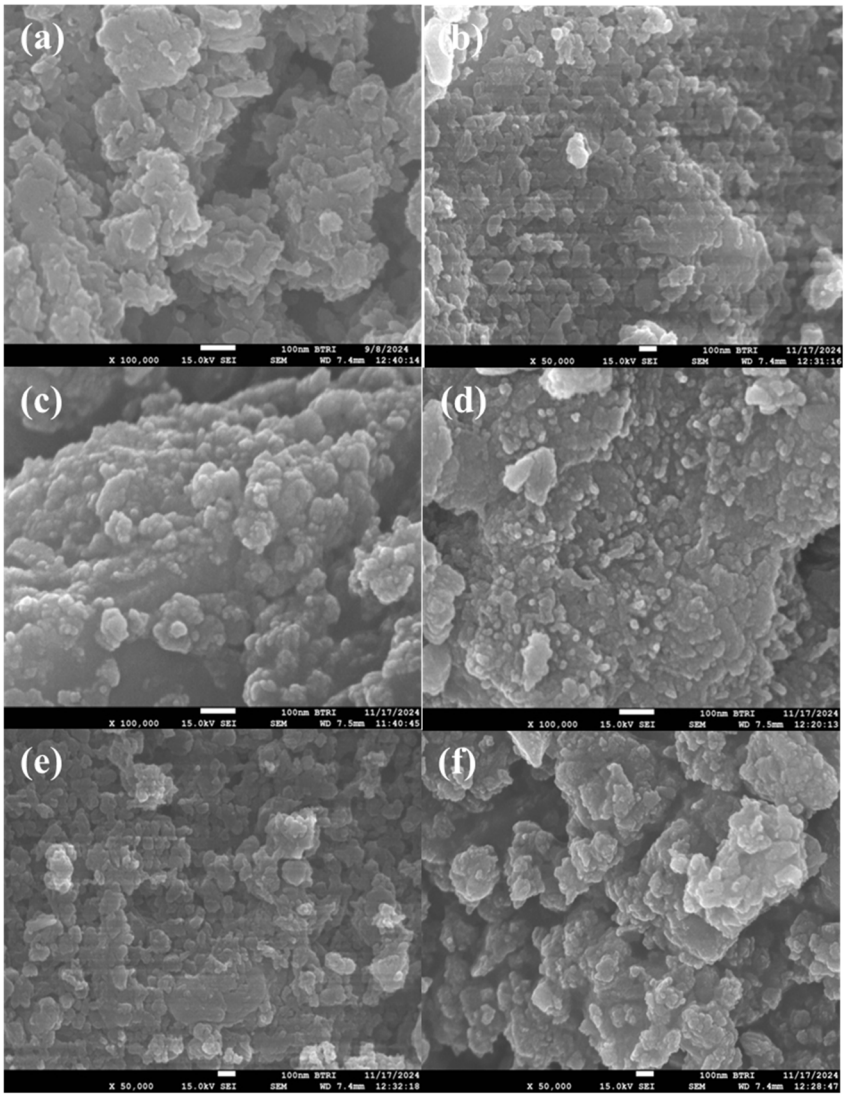

Fig. 5 SEM images of (a) clay, (b) CCN-1, (c) CCN-2, (d) CCN-3, (e) CCN-4, and (f) CCN-1 composite after Pb^{2+} adsorption.

where, Q_e (mg g^{-1}) = the amount of Pb^{2+} adsorbed onto the adsorbents at equilibrium, Q_m (mg g^{-1}) = the maximum Pb^{2+} adsorption capacity of the adsorbents, K_L (L mg^{-1}) = Langmuir constant, K_F (mg g^{-1}) (L $mg^{-1})^{1/n}$ = Freundlich constant, and K_T (L mg^{-1}) = Temkin constant.

3. Results and discussion

3.1 Characterizations

3.1.1 Fourier transform infrared spectroscopy (FTIR). The FT-IR analysis of the prepared clay and CCN is presented in Fig. 4(a and b). A total of four batches were prepared, and the

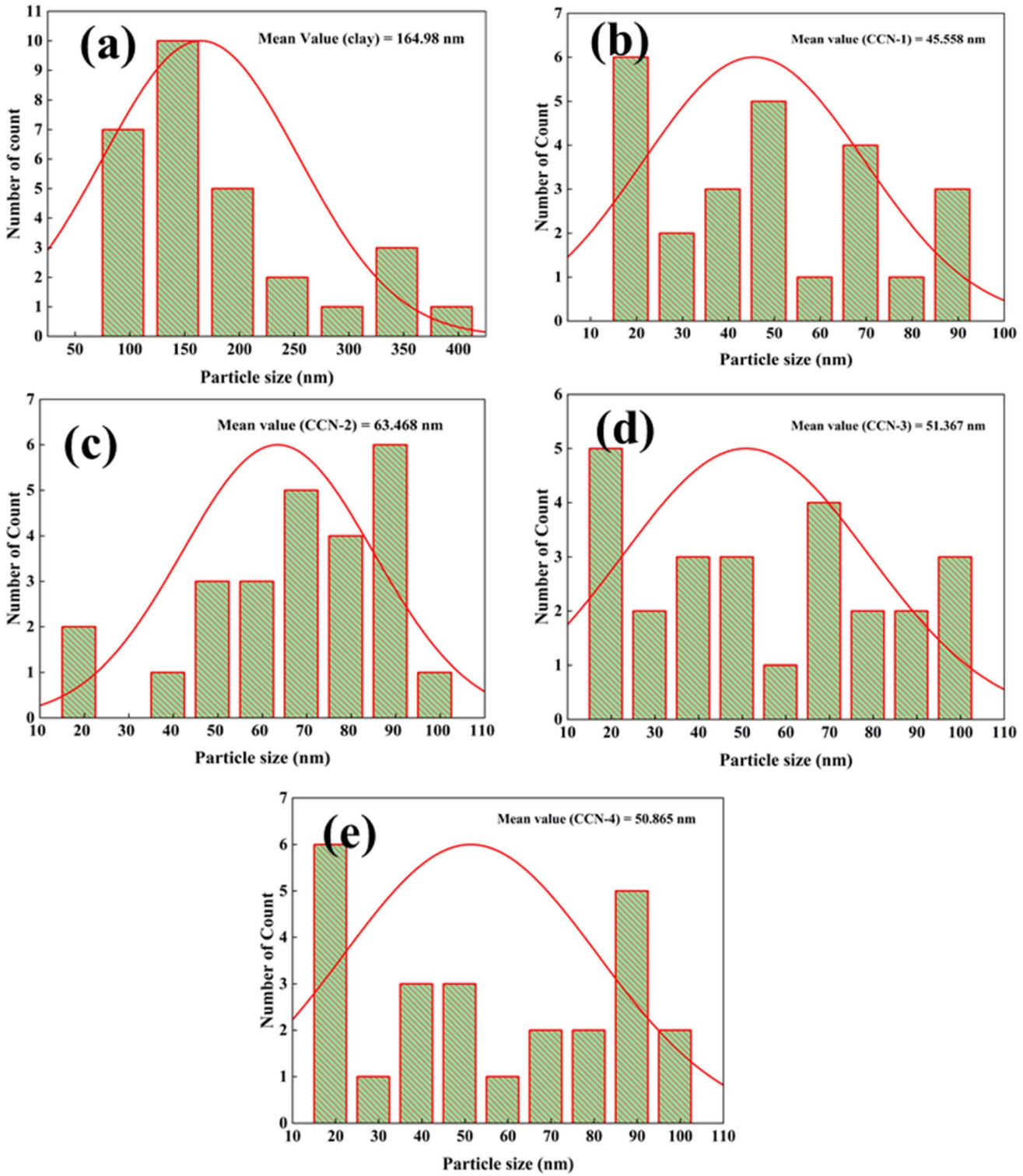

Fig. 6 Particle size calculation of (a) clay, (b) CCN-1, (c) CCN-2, (d) CCN-3, and (e) CCN-4.

data are presented here. In the region associated with O–H stretching, the clay sample displays a significant band within the wavenumber range of 3700–3600 cm^{-1}, which is attributed to OH stretching that is bonded to Al on the surface.[26] In the case of CCNs, at (3400–3100) cm^{-1}, the characteristic O–H stretching vibration peak is broad, which indicates the clay and cellulose were covered by each other.[27] The band at about ~1630 cm^{-1} could be attributed to the H–OH bonding, while the peak at about ~1402 cm^{-1} is for C–O stretching.[20,28] These peaks can be easily seen in Fig. 4(a). Furthermore, the band at ~1112 cm^{-1} refers to Si–O–Si, which is another indication of the formation of the composite.[29,30] In addition, peaks at ~1164, ~1059, ~1035, and ~695 cm^{-1} are for vibration of the $-SO_3H$ group, C–O–C vibration, Si–O vibration, and Si–O deformation,

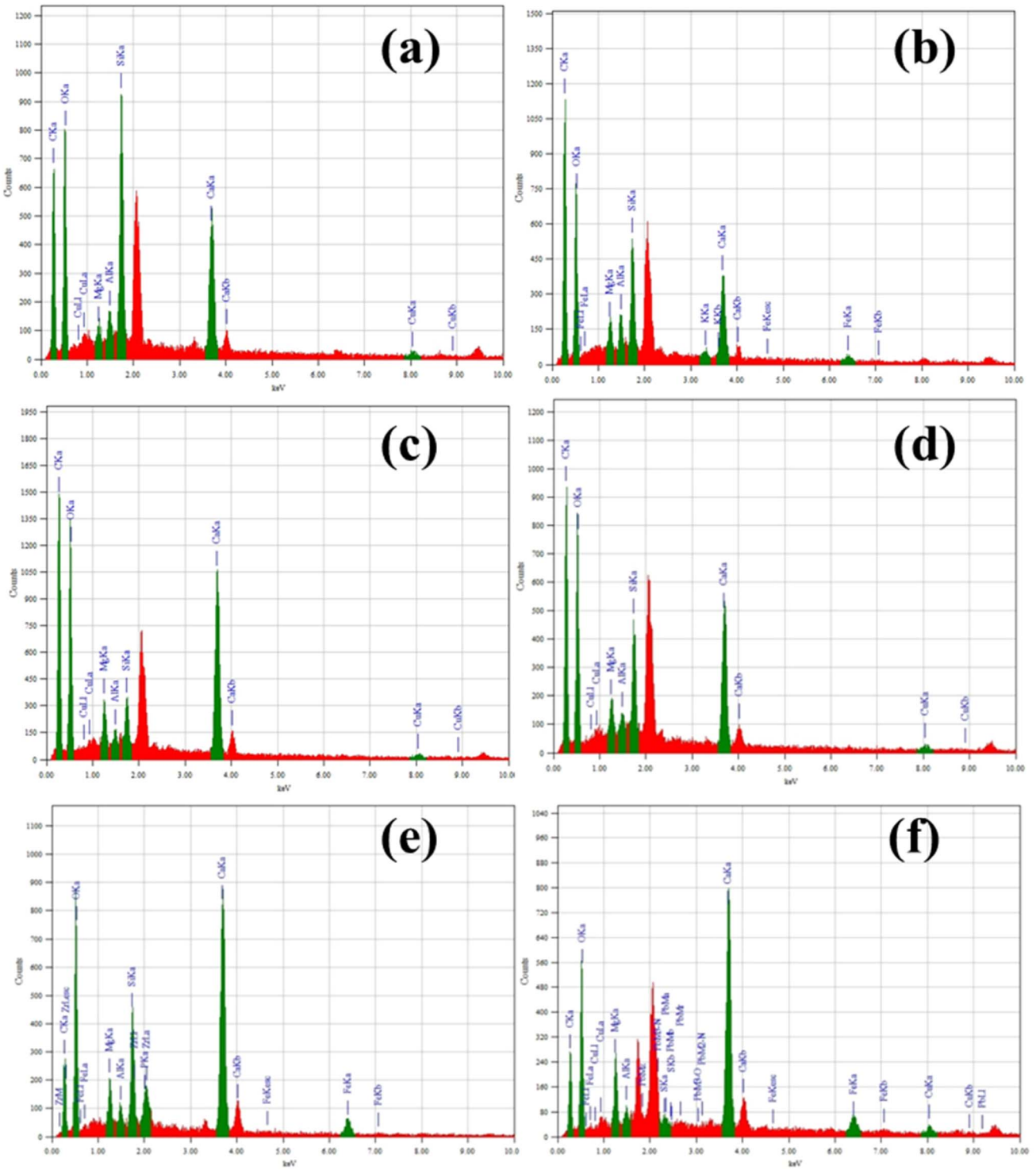

Fig. 7 EDX images of (a) clay, (b) CCN-1, (c) CCN-2, (d) CCN-3, (e) CCN-4, and (f) CCN-1 composite after Pb^{2+} adsorption.

respectively.[31] The absorption band detected around 874 cm^{-1} is associated with the β-glycosidic C–H deformation of cellulose, which may also include contributions from Al–OH or Si–O vibrations of the clay mineral, thereby confirming the effective creation of the cellulose–clay composite.[28] All these peaks in the region (1500–500) cm^{-1} are well seen from Fig. 4(b).

After Pb^{2+} adsorption, the change in the spectrum can be seen in the case of the CCN-1 sample. The broad, sharp characteristic O–H stretching vibration peak at (3400–3100) cm^{-1} exhibits a slight shift and a reduction in intensity, indicating successful binding of Pb^{2+} ions onto the composite surface.[32–34] After Pb^{2+} adsorption, the C–H stretching peak is observed at ~2904 cm^{-1} confirming the cellulose backbone remains structurally stable after metal adsorption. The peak at ~1630 cm^{-1} shows reduced intensity, suggesting interaction between the Pb^{2+} ion and carbonyl groups of cellulose or surface oxygen-containing groups. In the region (1200–1000) cm^{-1} the weakening of the $-SO_3H$ group, Si–O–Si vibration, and C–O–C vibration peaks indicate the participation of cellulose ether and alcohol groups in Pb^{2+} binding. The low intensity band at ~600 cm^{-1} after Pb^{2+} adsorption may be associated with Pb–O bonding, confirming the formation of lead–oxygen complexes on the composite surface.[32,35,36]

3.1.2 Scanning electron microscope (SEM). The clay's and CCNs' morphological characteristics are displayed in Fig. 5. The clay's SEM micrograph Fig. 5(a) indicates the existence of larger particles that appear to have been formed by several flaky particles coming together to create agglomerates.[26] It is clear from the SEM pictures that the composites in Fig. 5(b–e) do not contain any distinct cellulosic fiber. Furthermore, clay particles are also indistinguishable, which indicates the formation of the composite.[34]

The composites have compact, rough, and porous surfaces, and the particle size of the CCNs seems to be below 100 nm. During the CCN-1 synthesis, 6 g of clay was combined with 3 g of cellulose. This composite is observed to be of consistent size in relation to other batches. For other composites, the quantity of clay exceeded 6 g. The SEM images clearly show that the CCN-2, CCN-3, and CCN-4 composites exhibit agglomeration in comparison to CCN-1. This occurrence might result from the condition that 6 g of clay mixed with 3 g of cellulose is the ideal ratio for creating this composite. The 2 : 1 clay–cellulose ratio results from adequate cellulose coverage that stabilizes clay particles through hydrogen bonding, while increased clay loading surpasses cellulose's stabilizing ability, causing particle restacking and agglomeration. From Fig. 5(f), it can be seen that the particles are agglomerated together as a big particle after Pb^{2+} adsorption. CCN-1 composite was utilized in the Pb^{2+} adsorption experiment. It is clearly seen that, the almost uniform particles of CCN-1 (Fig. 5(b)) has been changed to non-uniform large particle (Fig. 5(f)). The particle size was calculated by ImageJ software and shown in Fig. 6. It can be seen that the average particle size of the treated clay sample was near 165 nm (Fig. 6(a)) whereas the particle sizes of the composites were 45.558 nm, 63.468 nm, 51.367 nm, and 50.865 nm for CCN-1, CCN-2, CCN-3 and CCN-4 respectively as can be seen in Fig. 6(b–e). CCN-1 exhibits the smallest particle size compared to others. The mean particle size of different batches was determined to be 52.81 ± 7.57 nm. The slight differences in particle size across batches can be linked to minor variations in synthesis conditions, including the dispersion efficiency of clay layers, the swelling behavior of cellulose, local differences in viscosity, and aggregation caused by drying during the formation of composites. Such slight variations between batches are frequently seen in polymer–clay nanocomposite systems because the nucleation and particle assembly are sensitive to the uniformity of mixing and interfacial hydrogen bonding. Statistical analysis indicates that the observed sizes are within one standard deviation of the overall mean, suggesting that the variations between batches fall within the normal range of experimental variability and do not indicate a significant alteration in particle formation behavior. In this study, the CCN-1 with the smallest particle size is considered because, with the decrease in the particle size, the surface area of the particles increases. This phenomenon aids in higher Pb^{2+} adsorption.[25]

3.1.3 Energy dispersive X-ray (EDX). Fig. 7 shows the EDX mapping data of clay, Fig. 7(a), and CCNs, Fig. 7(b–e). The silicon peak is prominent in the case of the clay, indicating the crucial element of the clay. The O also gives a major peak due to the presence of oxygen. The clay also contains traces of Mg^{2+}, Ca^{2+}, and Na^{+}, in oxide form, along with other elements in clay.[25] On the other hand, EDX mapping shows a broad peak of carbon for CCNs compared to clay, confirming the incorporation of cellulose. The peak for oxygen is strong for CCNs, as both clay and cellulose contain oxygen. There is a decrease in the Si peaks' intensity in the case of CCNs due to the dilution factor. It can be seen that, Ca^{2+}, Mg^{2+}, Si^{4+}, Al^{3+}, *etc.* are some of the major

Table 1 EDX elemental data of clay and CCNs

Element/mass%	Clay	CCN-1	CCN-2	CCN-3	CCN-4	CCN-1 after Pb^{2+} adsorption
Si	8.75	4.14	1.69	4.71	4.61	1.69
O	38.27	39.71	41.69	36.01	43.35	37.80
C	35.07	38.47	36.14	45.44	16.40	16.07
Al	0.97	0.50	0.48	1.47	0.86	0.65
Mg	0.74	1.43	1.71	1.29	2.02	3.95
Cu	4.63	3.25	2.46	—	—	6.39
Ca	11.57	12.50	—	—	2.54	25.19
Pb	—	—	—	—	—	2.87

elements of the nano-composites, which defends the combination of cellulose and clay within the nano-composite.[28] No new elements are detected for CCNs as no additives were used to prepare the CCNs. After Pb^{2+} adsorption, the presence of Pb can be seen in the CCN-1 composite as depicted in Fig. 7(f). The atom (%) of the clay, CCNs and CCN-1 after adsorption are listed in Table 1.

3.1.4 Zeta potential and point of zero charge (PZC). The zeta potential value and hydrodynamic diameter of the nano-composites at pH 6 are shown in Fig. 8. It is seen that, the CCN-1 demonstrated pH-sensitive zeta potential values that varied from −45.69 to +11.26 mV (Fig. 8(a)). At pH levels exceeding the PZC (3.65), the surface acquired a significant negative charge due to the deprotonation of surface hydroxyl

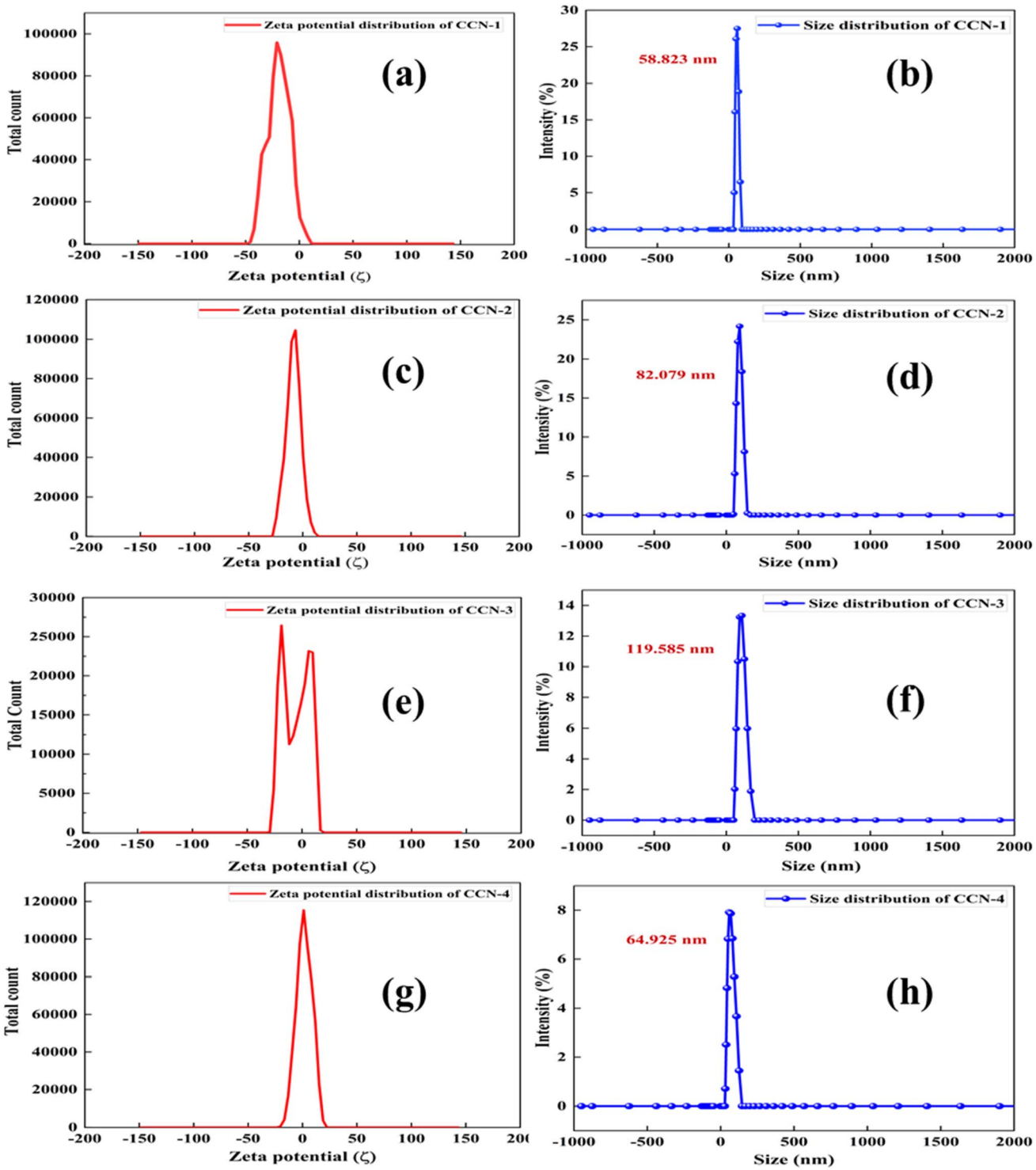

Fig. 8 Zeta potential of (a) CCN-1, (c) CCN-2, (e) CCN-3, (g) CCN-4, and hydrodynamic diameter of (b) CCN-1, (d) CCN-2, (f) CCN-3, (h) CCN-4 nano-composites at pH 6.

groups, leading to outstanding colloidal stability. The hydrodynamic diameter measured by DLS was around 58.823 nm (Fig. 8(b)), validating the nanoscale distribution of the composite in water. The presence of a high negative zeta potential along with a small hydrodynamic size suggests excellent dispersion stability and improved surface accessibility of CCN-1, both of which are beneficial for the adsorption of cationic heavy metals.[10,19] The zeta potential values of CCN-2, CCN-3, and CCN-4 are −24.53 to +11.07 mV, −29.36 to +16.9 mV, and −23.96 to +22.33 mV, respectively (Fig. 8(c), (e) and (g)). The hydrodynamic diameters are 82.079 nm, 119.585 nm, and 64.925 nm, respectively, for CCN-2, CCN-3, and CCN-4 batches (Fig. 8(d), (f) and (h)) indicate moderate dispersion stability.[19]

As the CCN-1 is more stable compared to other batches, the PZC value of CCN-1 was evaluated and is depicted in Fig. 9. The point of zero charge (PZC) for the CCN-1 was found to be pH 3.652, signifying that at this pH, the composite's surface has no net electrical charge. When the pH is below 3.652, the surface turns positively charged because of the protonation of functional groups, whereas above pH 3.652, the surface becomes negatively charged due to deprotonation. The relatively low PZC value suggests that the composite surface is acidic, which is due to the abundance of hydroxyl, silanol (Si–OH), and aluminol (Al–OH) functional groups derived from cellulose and clay minerals. These groups easily dissociate at pH levels higher than the PZC, resulting in negatively charged adsorption sites. When the solution pH exceeds the PZC, the surface of the nanocomposite retains a negative charge, promoting high electrostatic attraction and surface complexation with positively charged metal ions like (Pb^{2+}).[23]

3.1.5 Thermo-gravimetric analysis (TGA). To measure the thermal stability of the composites, TGA was performed. In the thermogram, there are two phases of degradation. Water was lost during the first stage between 40 °C and 150 °C. And then, a notable decrease in weight during the second stage, which is between 200 °C and 350 °C, appeared as shown in Fig. 10. This resulted from organic materials decomposing. The degradation temperature (T_{deg}) of the pure cellulose was about 269 °C,

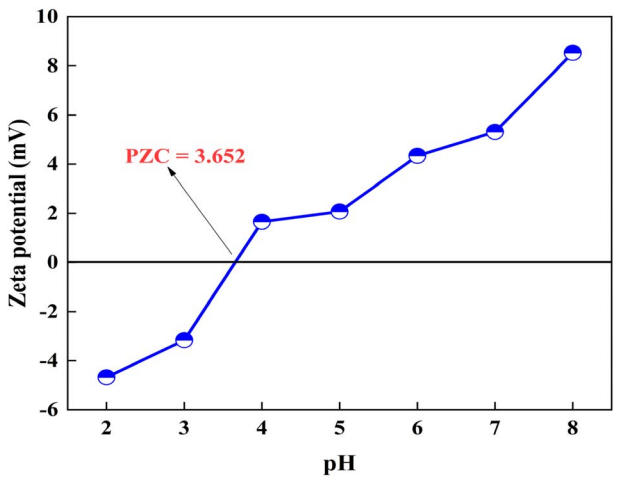

Fig. 9 Point of zero charge (PZC) of CCN-1.

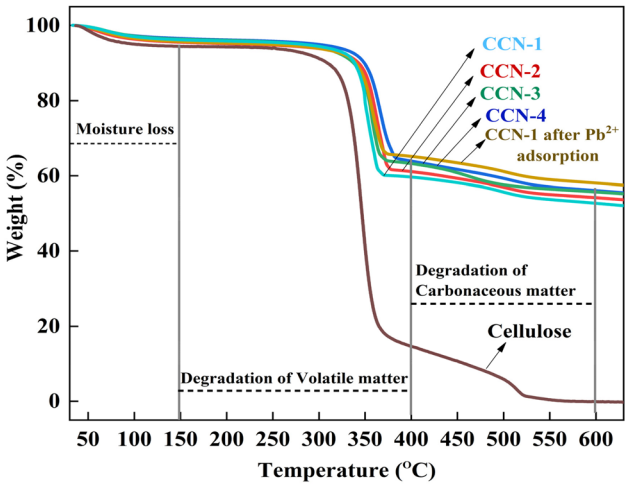

Fig. 10 TGA thermogram of cellulose and CCNs.

whereas in the case of the composites, the T_{deg} values were found above 310 °C, indicating increased resistance to thermal decomposition. The addition of clay to composites frequently results in such a notable increase in the composites' thermal stability. It seems that the exfoliated silicate sheets that formed as a result of the composite formation prevent the mechanism of thermal degradation of cellulose.[37]

The TGA curve for the CCN-1 composite following Pb^{2+} adsorption shows a minor rise in initial moisture loss and a transition of the primary cellulose degradation temperature to higher values, suggesting improved thermal stability as a result of robust Pb^{2+}–oxygen coordination. The greater residual mass (~58%) compared to the residual mass of CCN-1 (~52%) further validates the effective Pb^{2+} loading onto the composite.[37]

3.1.6 X-ray diffraction (XRD) analysis. Sharp and pointed diffraction peaks are observed for the prepared CCNs from the XRD data, as depicted in Fig. 11. The corresponding peaks are $2\theta = 20.838°$, 22.810°, 26.637°, 29.374°, 45.780°, and 81.480° for CCN-1, $2\theta = 20.850°$, 22.860°, 26.615°, 29.373°, and 81.407° for CCN-2, $2\theta = 20.820°$, 22.640°, 26.613°, 29.337°, 45.696°, and 81.458° for CCN-3 and $2\theta = 20.888°$, 22.610°, 26.675°, 29.407°, 45.837°, and 81.130° for CCN-4 respectively.[7,20] These sharp peaks indicate the crystalline nature of the composites. From these sharp peaks, it can also be said that the clay layer in the CCN might be orderly distributed.[20] The clays are rendered more organophilic due to surface alteration, enhancing their interaction with the biopolymer cellulose and resulting in a fine dispersion within the matrix.[7] The XRD pattern for the CCN-1 composite following Pb^{2+} adsorption reveals a minor shift and decrease in intensity of the distinct peaks associated with both clay and cellulose, suggesting that interlayer expansion and an increase in structural disorder have occurred due to the intercalation of Pb^{2+} and surface complexation. The lack of crystalline Pb phases indicates that lead is present in an amorphous state as opposed to being precipitated.[20]

The crystallite size, crystallinity, and dislocation density of the composites are determined by the following equations and are depicted in Table 2.

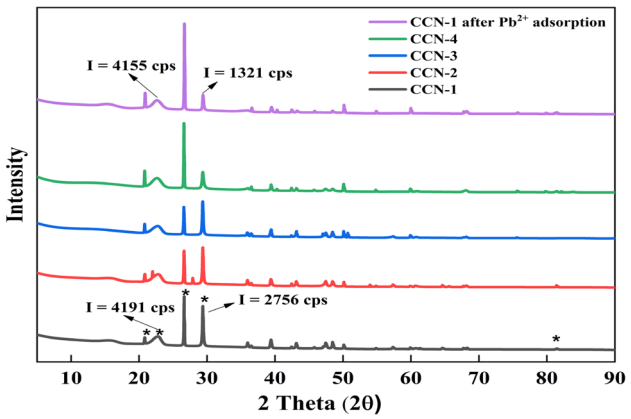

Fig. 11 XRD pattern of prepared CCNs.

$$\text{Crystallite size, } D = \frac{k\lambda}{\beta \cos\theta} \quad (9)$$

$$\text{Crystallinity } (\%) = \frac{I_{(1)}}{I_{(1)} + I_{(2)} + I_{(3)}} \quad (10)$$

$$\text{Dislocation density, } \delta = \frac{1}{D^2} \quad (11)$$

From Table 2, it can be seen that CCN-1 nano-composite has the smallest average crystallite size and high crystallinity, which makes CCN-1 more prominent than the other batches.

Table 2 Size of the crystallite, dislocation density, and crystallinity of the CCNs

Composites	Average crystallite size, D (nm)	Dislocation density, δ	Crystallinity (%)
CCN-1	63.833	2.45×10^{-4}	69.03%
CCN-2	72.904	1.88×10^{-4}	63.88%
CCN-3	55.873	3.20×10^{-4}	63.47%
CCN-4	72.881	1.88×10^{-4}	50.64%

3.1.7 UV-vis analysis. Fig. 12(a) describes the UV spectra of pure cellulose and the prepared batches of CCNs. It is seen that the absorption maxima (λ_{max}) is at 211 nm for pure cellulose. In the case of the CCCs, the absorption maxima shifted to 353, 345, 346, and 344 nm, respectively, for CCN-1, CCN-2, CCN-3, and CCN-4. The development of the composite may be the cause of this red shift. In Fig. 12(b) the band gap calculation is shown based on Tauc plot. It is seen that the cellulose has a higher band gap of 4.427 eV compared to the composites (CCN-1 = 3.150 eV; CCN-2 = 3.137 eV; CCN-3 = 3.239 eV, and CCN-4 = 3.195 eV). The lower band gap of the composites is generally attributed to high structural disorder and strong interfacial bonding between clay layers and cellulose chains. These increased defects on the composite act as coordination sites for Pb^{2+} adsorption, resulting in higher Pb^{2+} adsorption capacity. Generally, the –OH, –COOH groups of cellulose and the –Si–O$^-$, –Al–O$^-$ groups of clay show electronic interaction with Pb^{2+} when the band gap is smaller due to easy charge transfer.[38–40]

3.2 Adsorption kinetic study

From the above discussion, the CCN-1 batch was found to be preferable than other batches. So, the adsorption study was carried out using CCN-1 nano-composite.

3.2.1 Dosage effect. Fig. 13(a) illustrates the findings about the dosage effect on the elimination of Pb^{2+}. The adsorption procedure lasted for 60 minutes at 6.0 pH, 30 ± 0.5 °C, and a Pb^{2+} concentration of 100 mg L^{-1}. The adsorbents from 0.05 to 0.15 g were employed to assess their adsorption capabilities.

The figure illustrates that the adsorption capacity of Pb^{2+} by composites rose as the dosage increased up to a specific level, after which it gradually declined. Conversely, the removal capacity improved with CCN dosage enhancement and eventually stabilized. The maximum removal of Pb^{2+} recorded was 98.71% with a capacity of 197.42 mg g^{-1} at a CCNs dosage of 0.1 g.

The relationship between higher adsorbent dosage and enhanced removal efficiency is explained by the rise in active

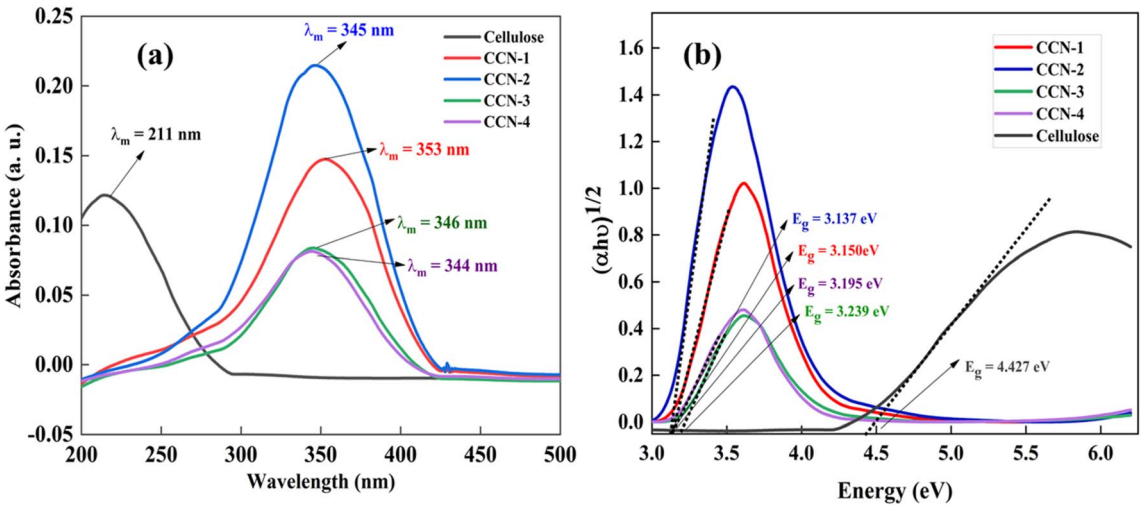

Fig. 12 (a) UV spectra, and (b) band-gap of cellulose and prepared CCNs.

adsorption sites as the quantity of adsorbent increases. However, since the Pb^{2+} concentration in the solution stayed the same, this led to a surplus of unoccupied adsorption sites that were not fully utilized, and a decline in adsorption capacity is observed after a certain point.[41,42]

3.2.2 Effect of time of contact. Pb^{2+} ions adsorption by CCN-1s was studied against time, and the findings are shown in Fig. 13(b). Using CCN as an adsorbent led to an increase in the adsorption of Pb^{2+} over time. The CCN's adsorbent reached equilibrium in 60 minutes, and a notable rapid adsorption during the initial 60 minutes was also recorded, achieving a higher removal efficiency for Pb^{2+} of 97.9% for 100 mg L^{-1}. This outcome highlighted the significant effect of CCNs on the adsorption process. Initially, Pb^{2+} ion adsorption increased due to the huge availability of active sites for binding. So, the adsorption rate went up steadily until it reached equilibrium.

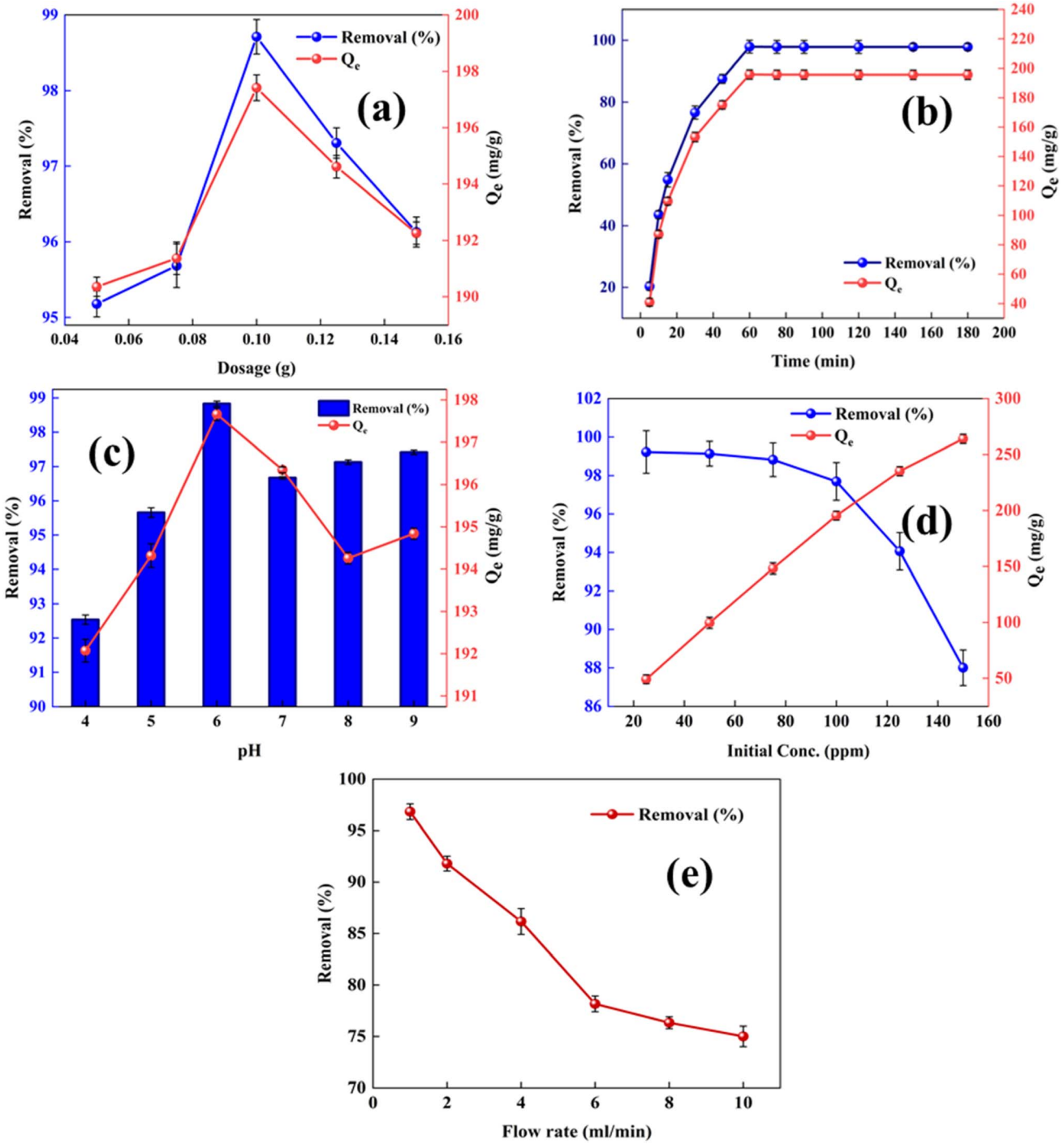

Fig. 13 (a) Dosage effect, (b) effect of time of contact, (c) pH effect, (d) effect of initial Pb^{2+} concentration, and (e) effect of flow rate of CCN on the Pb^{2+} removal.

Following the specified duration, the adsorption process became stable, indicating that equilibrium had been achieved.

3.2.3 Effect of pH. Fig. 13(c) illustrates how pH affects the adsorption of Pb^{2+} metal ions by CCNs in the pH range of 4–9. The pattern indicates that pH has a major impact on CCNs' capacity for adsorption. The efficacy of adsorption processes is strongly governed by the initial pH value.[43] The removal efficiency of Pb^{2+} by CCNs adsorbent showed a proportional increase with pH values; at pH 6, the maximum Pb^{2+} ion removal was 98.83%. This is explained by the fact that changes in pH affect the surface charge of CCNs, which in turn affects the rate of removal.[44]

On the surface of the CCN's adsorbent, a considerable quantity of Pb^{2+} competes for the active adsorption sites when the pH values are lower. Due to the higher positive charge on the adsorbent surface, Pb^{2+} finds it challenging to find sufficient negative charge to bind efficiently. Because Pb^{2+} and the positively charged CCNs adsorbent surface are electrostatically repelled, the removal rate is comparatively low. The composite's capacity to eliminate metal ions was limited at low pH values. The capacity of adsorption was lower due to hydrogen ions competing with Pb^{2+} ions at low pH values.[45] A higher adsorption capacity facilitated by electrostatic attraction results from the surface charge of CCNs adsorbent shifting towards a more negative state as pH rises, and the competitive adsorption between the Pb^{2+} ions and H^{+} ions also reduces significantly.[7] At higher pH values, a decrease in adsorption was seen, most likely as a result of hydroxide complex formation.[45]

3.2.4 Effect of initial Pb^{2+} ions concentration. The effectiveness of adsorption was investigated at different concentrations of Pb^{2+} at the optimum time of 60 minutes.

Fig. 13(d) reveals that the Pb^{2+} adsorption showed a decreasing trend as the initial metal ion concentration increased. The efficiency of Pb^{2+} removal at different Pb^{2+} concentrations from 25 to 150 mg L^{-1} by the designed column with layers of 0.1 g of CCNs adsorbent. 99.22%, 99.13%, 98.82%, 97.69%, 94.06%, and 88.00% of Pb^{2+} were successfully eliminated by the column containing 25, 50, 75, 100, 125, and 150 mg L^{-1} of Pb^{2+} ions, respectively. Though the concentration of initial Pb^{2+} increases, the active sites of the adsorbent remain the same. Thus same amount of adsorbent becomes less efficient for higher concentration solution resulting in decreased removal.[45]

3.2.5 Effect of rate of flow on Pb^{2+} adsorption in column. By altering the rate of flow from 1 to 10 mL min^{-1}, the effect of flow rate on the Pb^{2+} adsorption in a packed column was investigated. The initial Pb^{2+} concentration was kept at

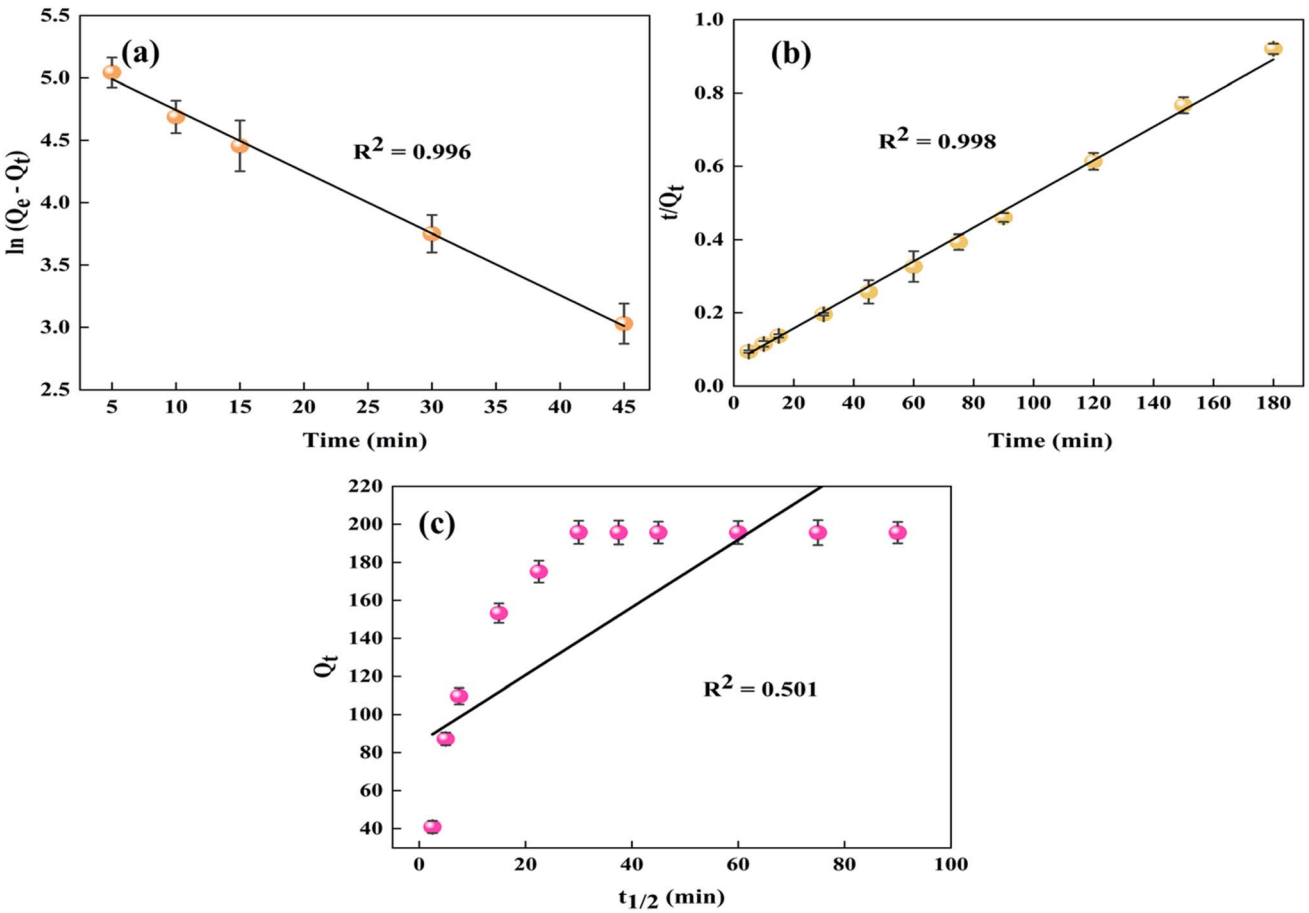

Fig. 14 (a) Pseudo-first order kinetic model, (b) pseudo-second order kinetic model, and (c) intra-particle diffusion method for adsorptions of Pb^{2+} from aqueous solution by the CCN-1.

Table 3 Kinetic parameters obtained for pseudo-first order, pseudo-second order, and intra-particle diffusion kinetics on Pb^{2+} adsorption

Kinetic model	Parameters	Pb(II) ion
Pseudo-first order	$Q_{e,exp.}$ (mg g^{-1})	195.801
	$Q_{e,cal.}$ (mg g^{-1})	185.718
	k_1 (min^{-1})	−0.0003
	R^2	0.996
Pseudo-second order	$Q_{e,exp.}$ (mg g^{-1})	195.801
	$Q_{e,cal.}$ (mg g^{-1})	204.081
	k_2 (g mg^{-1} min^{-1})	0.0004
	R^2	0.998
Intra-particle diffusion	R^2	0.501

Table 4 Adsorption isotherm parameters obtained for Pb^{2+}

Isotherm model	Parameter	Pb(II) ion
Langmuir	$Q_{e,exp.}$ (mg g^{-1})	195.39
	$Q_{e,cal.}$ (mg g^{-1})	198.41
	K_L (L g^{-1})	1.556
	R^2	0.999
Freundlich	K_F (mg g^{-1}) (L $mg^{-1})^{1/n}$	61.151
	N	2.931
	R^2	0.833
Temkin	B_T (J mol^{-1})	2.83412
	K_T (L mg^{-1})	17.6468
	R^2	0.971

100 mg L^{-1} at pH = 6, and at 30 ± 0.5 °C throughout the experiments.

As expected, the Pb^{2+} adsorption decreased with increased flow rate, as shown in Fig. 13(e). The removal (%) decreased from 96.83% to 75% for 1–10 mL flow rate. Generally speaking, a faster flow rate reduces the time that the Pb^{2+} ions and column material are in contact. Conversely, a slower flow allows the Pb^{2+} ions and the column material to come into contact for a longer period of time, increasing the column's removal efficiency.

3.3 Kinetics study of Pb^{2+} adsorption

Fig. 14 displays different adsorption kinetics model fitting, while Table 3 presents the calculated parameters for pseudo-first, pseudo-second order, and intra-particle diffusion kinetic models. For the adsorption of Pb^{2+} onto the adsorbents, it was evident from the correlation coefficient (R^2) that the pseudo-second order kinetic model (R^2 = 0.998) offered a better

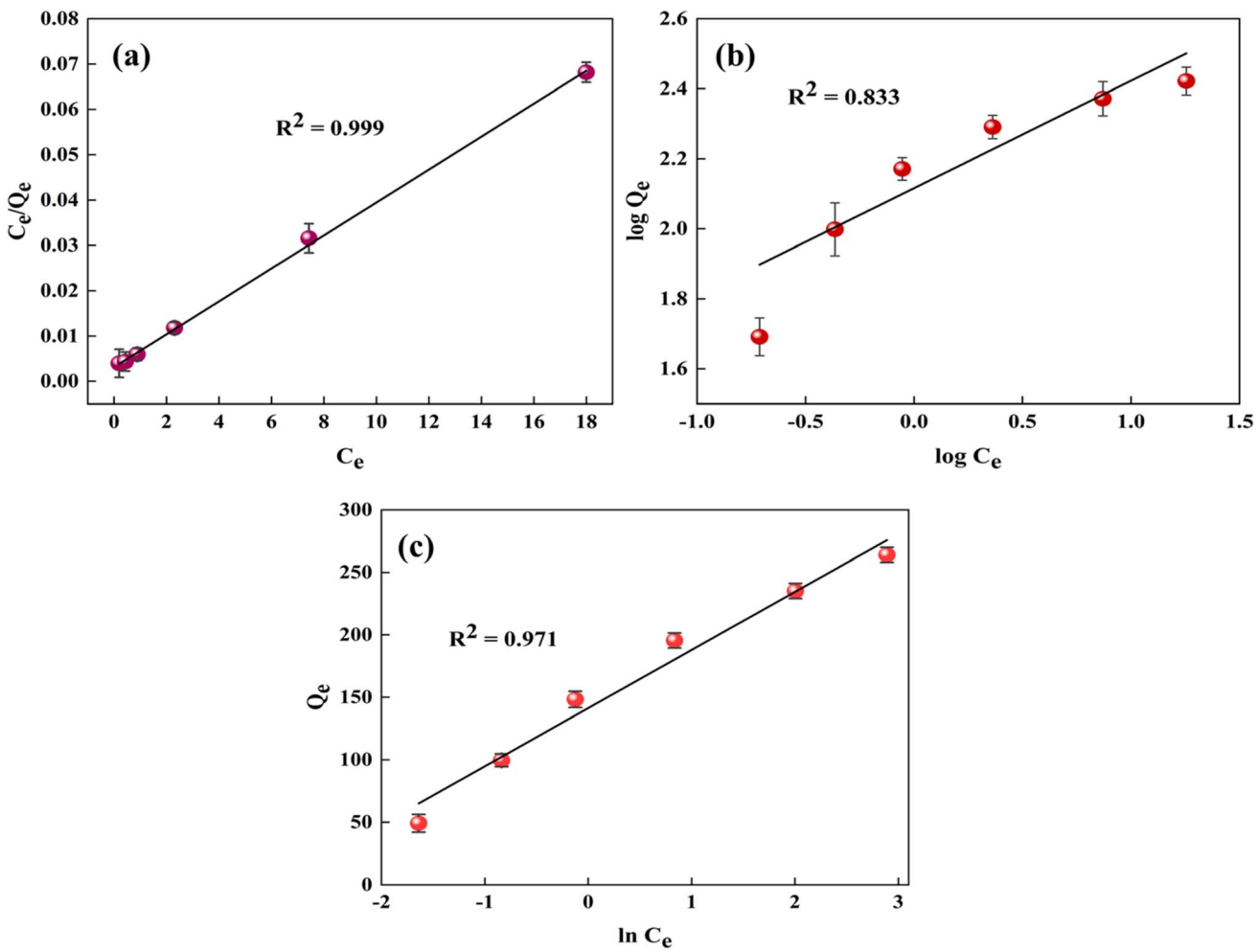

Fig. 15 (a) Langmuir, (b) Freundlich, and (c) Temkin adsorption isotherms for adsorptions of Pb^{2+} from aqueous solution by the CCN-1.

Table 5 Comparison of CCN-1 maximum Pb^{2+} ion removal efficiency with other adsorbents

Adsorbents	Adsorption condition	Adsorption condition	Removal capacity (mg g^{-1})	Optimum kinetic	Optimum isotherm
Sodium-alginate–cellulose–nano-clay composite[49]	Batch adsorption	5.5, 25 °C	0.11	Pseudo-second order	Langmuir
Bentonite–cellulose hydrogel[50]	Batch adsorption	6.0, 25 °C	110.64	Pseudo-second order	Sips
Cellulose nanoparticles/chitosan composition[48]	Batch adsorption	6.0, 25 °C	221.104	Pseudo-second order	Langmuir
Clay modified sodium carboxymethyl cellulose[51]	Batch adsorption	7.0, 25 °C	5.1	—	Freundlich
Biosorbent[53]	Packed column	6.0, 25 °C	108	Pseudo-second order	Langmuir
Cellulose/zeolite-A composite[52]	Batch adsorption	6.5, 25 °C	94.51	Pseudo-second order	Langmuir
Biomass/resin mixture[54]	Packed column	5.0, 25 °C	62.96	—	Langmuir
Biochar derived from poplar saw dust[55]	Batch adsorption	5.0, 25 °C	62.68	—	Langmuir
CCN (this study)	Packed column	6.0, 30 °C	195.80	Pseudo-second order	Langmuir

correlation than the pseudo-first order ($R^2 = 0.996$) and intra-particle diffusion ($R^2 = 0.501$).

The pseudo-second-order model of the adsorption kinetics suggests that the chemical interactions between the Pb^{2+} ions and the CCNs' active sites control the adsorption rate. The results of the determination of the adsorption rate constant indicate that CCNs have quick adsorption kinetics, which makes them appropriate for a quick water treatment process.[46–48]

3.4 Adsorption isotherm study

Adsorption isotherms, which offer vital information, were used to assess the prepared adsorbent's effectiveness for Pb^{2+} adsorption. The Langmuir, Freundlich, and Temkin isotherm models were used to study the obtained data, and Fig. 15 shows the corresponding plots. The parameters derived from fitting these models to the experimental data are shown in Table 4. According to Table 4, correlation coefficient (R^2) values were 0.999 (Langmuir), 0.833 (Freundlich), and 0.971 (Temkin) for the isotherm models, respectively. These values may indicate that this study followed the Langmuir model of adsorption, indicating monolayer surface adsorption.[46,47]

In Table 5, the comparison of the Pb^{2+} adsorption capacity of our prepared CCN-1 with other composites is summarized. Compared to the adsorption capacity of other adsorbents, this newly synthesized CCN-1 adsorbent demonstrates reliable and impressive adsorption capacity.

While this study demonstrates the high efficiency of the composite for Pb^{2+} ions removal, certain limitations should be acknowledged. This research was carried out in a controlled laboratory setting using single-metal aqueous solutions. Although the suggested CCN shows encouraging adsorption performance, additional efforts are necessary to assess regeneration capabilities, and long-term column stability in actual wastewater systems. Subsequent studies need to assess the adsorption capabilities of the created CCN in multi-metal systems and actual wastewater matrices with competing ions, dissolved organic compounds, and suspended contaminants. Extended regeneration studies and adsorption–desorption cycling are essential to assess the structural stability and cost-effectiveness of the composite for multiple applications. Moreover, altering the CCN surface *via* chemical activation, adding nanoparticles, or adjusting pore structures could further improve adsorption selectivity and capacity for wider heavy-metal remediation uses. Further research involving real wastewater applications and composite recyclability is currently underway. These findings will be reported in a forthcoming publication.

4. Conclusion

To summarize, the development of a novel cellulose–clay nanocomposite (CCN) from a unique clay source is reported for the first time as a prominent adsorbent for the effective capture of lead (Pb^{2+}) from water. The characterization of the CCN using state-of-the-art techniques such as FTIR, XRD, SEM-EDX, TGA, and UV-vis spectroscopy provided essential insights into the formation of the composite material. A controlled adsorption method was utilized to assess the influence of pH, temperature, initial Pb^{2+} ion concentration, contact time, adsorbent dosage, and the flow rate on the removal efficiency of the CCN under competitive circumstances. The ideal conditions were found to be a pH of 6.0, a contact time of 60 min, a temperature of 30 °C, an initial Pb^{2+} concentration of 0.1 mg L^{-1}, an adsorbent dosage of 5 mg L^{-1}, and a flow rate of 1 mL min^{-1}. Under these conditions, the CCN demonstrates an impressive adsorption capacity of 195.80 mg g^{-1} when utilized in the designed packed column adsorption system. At an optimal temperature of 30 °C, the experimental results correspond well to the Langmuir adsorption isotherm model ($R^2 = 0.999$) and exhibit strong conformity with pseudo-second order kinetics ($R^2 = 0.998$), validating the occurrence of spontaneous monolayer adsorption *via* a chemical adsorption mechanism. These findings could encourage the advancement of novel adsorbents aimed at eliminating heavy metals from wastewater.

Author contributions

Mirza Nusrat Sweety: investigation, methodology, formal analysis, data analysis, writing – original draft and editing;

Shamima Akther Eti: conceptualization, supervision, methodology, investigation, writing – review and editing; Muhammad Amirul Hoque: writing – reviewing and editing, data curation; Mohammad Shahid Ullah: writing – reviewing and editing, data curation; Shabiba Parvin Shandhi: methodology, investigation, data analysis; Fariha Chowdhury: data analysis; Md. Khabir Uddin Sarker: writing – reviewing and editing, data curation; Sarna Khanam: methodology, investigation; Farid Ahmed: writing – reviewing and editing, data analysis; Mohammad Mahbubur Rahman: idea generation, conceptualization, supervision, validation, funding acquisition, writing – review and editing.

Conflicts of interest

The authors declare that they have no known competing financial interests or personal relationships that could have appeared to influence the work reported in this paper.

Data availability

All data supporting the findings of this study are included in the main manuscript. Raw data are available from the corresponding author upon reasonable request.

Acknowledgements

We gratefully acknowledge the Bangladesh Council of Scientific and Industrial Research (BCSIR) for the financial support of this research.

References

1 M. Ahmad, S. Ahmed, B. L. Swami and S. Ikram, Adsorption of heavy metal ions: role of chitosan and cellulose for water treatment, *Langmuir*, 2015, **79**, 109–155.
2 Z. Zhang, Y. Lu, S. Gao and S. Wu, Sustainable and efficient wastewater treatment using cellulose-based hydrogels: a review of heavy metal, dye, and micropollutant removal applications, *Separations*, 2025, **12**(3), 72.
3 R. A. Goyer and T. W. Clarkson, Toxic effects of metals, *Casarett and Doull's Toxicology: The Basic Science of Poisons*, 1996, vol. 5, pp. 691–736.
4 K. Y. Foo and B. H. Hameed, Insights into the modeling of adsorption isotherm systems, *Chem. Eng. J.*, 2010, **156**(1), 2–10.
5 S. Deng, Adsorption of heavy metals onto biochar: A review, *Environ. Sci. Technol.*, 2020, **54**(10), 6028–6044.
6 R. Ahmad and A. Mirza, Adsorption of heavy metal ions using polymer-based composites: A review, *Environ. Sci. Pollut. Res.*, 2019, **26**(9), 8444–8466.
7 E. Abu-Danso, S. Peräniemi, T. Leiviskä, T. Kim, K. M. Tripathi and A. Bhatnagar, Synthesis of clay-cellulose biocomposite for the removal of toxic metal ions from aqueous medium, *J. Hazard. Mater.*, 2020, **381**, 120871.
8 V. K. Gupta, A. Nayak and S. Agarwal, Bioadsorbents for remediation of heavy metals: current status and their prospects, *Environ. Eng. Res.*, 2015, **20**(1), 1–18.
9 S. A. Khan, Bio-based adsorbents for heavy metal removal: A review, *Environ. Chem. Lett.*, 2021, **19**(6), 4747–4769.
10 M. K. Uddin, A review on the adsorption of heavy metals by clay minerals, with special focus on the past decade, *Chem. Eng. J.*, 2017, **308**, 438–462.
11 P. Kanmani, J. Aravind, M. Kamaraj, P. Sureshbabu and S. Karthikeyan, Environmental applications of chitosan and cellulosic biopolymers: A comprehensive outlook, *Bioresour. Technol.*, 2017, **242**, 295–303.
12 D. Klemm, D. Schumann, F. Kramer, N. Heßler, M. Hornung, H. P. Schmauder and S. Marsch, Nanocelluloses as innovative polymers in research and application, *Polysaccharides II*, 2006, pp. 49–96.
13 R. Sabarish and G. Unnikrishnan, Polyvinyl alcohol/carboxymethyl cellulose/ZSM-5 zeolite biocomposite membranes for dye adsorption applications, *Carbohydr. Polym.*, 2018, **199**, 129–140.
14 R. Sabarish, J. Karayil, J. Parameswaranpillai and S. Siengchin, Adsorption of methylene blue dye from aqueous solution by a novel PVA/CMC/halloysite nanoclay bio composite: Characterization, kinetics, isotherm and antibacterial properties, *J. Environ. Health Sci. Eng.*, 2020, **18**(2), 1311–1327.
15 R. Sabarish, J. Karayil, A. Jayakumar, J. Parameswaranpillai and S. Siengchin, An efficient removal of malachite green dye from aqueous environment using ZSM-5 zeolite/polyvinyl alcohol/carboxymethyl cellulose/sodium alginate bio composite, *J. Polym. Environ.*, 2021, **29**(7), 2126–2139.
16 I. Wilson, Applied Clay Mineralogy. Occurrences, processing and application of kaolins, bentonite, palygorskitesepiolite, and common clays, Haydn H. Murray. Developments in Clay Science, *Clays Clay Miner.*, 2007, **55**(6), 644–645.
17 D. H. K. Reddy and S. M. Lee, Application of magnetic chitosan composites for the removal of toxic metals and dyes from aqueous solutions, *Adv. Colloid Interface Sci.*, 2013, **201–202**, 68–93.
18 H. H. Murray, *Applied Clay Mineralogy: Occurrences, Processing and Applications of Kaolins, Bentonites, Palygorskitesepiolite, and Common Clays*, Elsevier, 2006.
19 B. K. G. Theng, Clay-polymer interactions: Summary and perspectives, *Clay Miner.*, 2012, **47**(1), 23–28.
20 A. S. K. Kumar, S. Kalidhasan, V. Rajesh and N. Rajesh, Application of cellulose-clay composite biosorbent toward the effective adsorption and removal of chromium from industrial wastewater, *Ind. Eng. Chem. Res.*, 2012, **51**(1), 58–69.
21 J. Wang and X. Guo, Adsorption kinetic models: Physical meanings, applications, and solving methods, *J. Hazard. Mater.*, 2020, **390**, 122156.
22 H. Kandil and S. T. El-Wakeel, Effective removal of Pb(II) and Cu(II) from aqueous solutions using a hybrid composite of fuller's earth, aluminum silicate, and chitosan, *Polym. Bull.*, 2024, **81**, 1839–1859.

23 H. Zhou, H. Zhu, F. Xue, H. He and S. Wang, Cellulose-based amphoteric adsorbent for the complete removal of low-level heavy metal ions via a specialization and cooperation mechanism, *Chem. Eng. J.*, 2020, **385**, 123879.

24 Y. Vieira, J. M. N. dos Santos, J. S. Piccin, Á. Bonilla-Petriciolet and G. L. Dotto, Adsorption as an Efficient Alternative for the Removal of Toxic Metals from Water and Wastewater, in *Toxic Metals Contamination*, 2022, pp. 146–171.

25 S. Khanam, S. A. Eti, M. S. Bashar, S. A. Sujan, N. Sharmin and S. K. Ray, Dynamic absorption of heavy metal from aqueous solution using lignin-hydrogel and natural filter materials in a packed column system, *Int. J. Biol. Macromol.*, 2025, **302**, 140356.

26 A. Kourim, M. A. Malouki, A. Ziouche, M. Boulahbal and M. Mokhtari, Tamanrasset's Clay Characterization and Use as Low-Cost, Ecofriendly, and Sustainable Material for Water Treatment: Progress and Challenge in Copper Cu(II), *Defect Diffus. Forum*, 2021, **406**, 457–472.

27 P. Sirajudheen, P. Karthikeyan, M. C. Basheer and S. Meenakshi, Adsorptive removal of anionic azo dyes from effluent water using Zr(IV) encapsulated carboxymethyl cellulose-montmorillonite composite, *Environ. Chem. Ecotoxicol.*, 2020, **2**, 73–82.

28 M. E. Abd El-Aziz, K. H. Kamal, K. A. Ali, M. S. Abdel-Aziz and S. Kamel, Biodegradable grafting cellulose/clay composites for metal ions removal, *Int. J. Biol. Macromol.*, 2018, **118**, 2256–2264.

29 A. B. Moustafa, M. E. Abd El-Aziz, A. M. Rabea and H. A. Essawy, Polystyrene-montmorillonite core–shell particles via Pickering emulsion polymerization and their use as reinforcing additives for polypropylene and ethylene vinyl acetate, *Polym. Eng. Sci.*, 2015, **55**(7), 1546–1552.

30 S. P. Santoso, A. Kurniawan, F. E. Soetaredjo, K. C. Cheng, J. N. Putro, S. Ismadji and Y. H. Ju, Eco-friendly cellulose–bentonite porous composite hydrogels for adsorptive removal of azo dye and soilless culture, *Cellulose*, 2019, **26**, 3339–3358.

31 A. Kausar, R. Shahzad, S. Asim, S. Bibi, J. Iqbal, N. Muhammad, M. Sillanpaa and I. U. Din, Experimental and theoretical studies of Rhodamine B direct dye sorption onto clay-cellulose composite, *J. Mol. Liq.*, 2021, **328**, 115165.

32 S. Babel and T. A. Kurniawan, Low-cost adsorbents for heavy metals uptake from contaminated water: A review, *J. Hazard. Mater.*, 2003, **97**, 219–243.

33 K. Nakamoto, M. Ohshiro and T. Kobayashi, Mordenite zeolite—Polyethersulfone composite fibers developed for decontamination of heavy metal ions, *J. Environ. Chem. Eng.*, 2017, **5**(1), 513–525.

34 K. Nakamotoa, M. Ohshirob and T. Kobayashia, Continuous flow column adsorption of mordenite zeolite–polymer composite fibers for lead removal, *Desalin. Water Treat.*, 2018, **109**, 297–306.

35 V. K. Gupta and I. Ali, *Environmental Water: Advances in Treatment, Remediation and Recycling*, Newnes, 2012.

36 M. A. Hubbe, S. H. Hasan and J. J. Ducoste, Cellulosic substrates for removal of pollutants from aqueous systems: A review. Metals, *BioResources*, 2011, **6**(2), 2161–2287.

37 M. M. Islam, M. N. Khan, S. Biswas, T. R. Choudhury, P. Haque, T. U. Rashid and M. M. Rahman, Preparation and characterization of Bijoypur clay-crystalline cellulose composite for application as an adsorbent, *Adv. Mater. Sci.*, 2017, **2**(3), 1–7.

38 G. Liu, X. Zhang, H. Liu, Z. He, P. L. Show, Y. Vasseghian and C. Wang, Biochar/layered double hydroxides composites as catalysts for treatment of organic wastewater by advanced oxidation processes: a review, *Environ. Res.*, 2023, **234**, 116534.

39 L. Zhu, D. Shen and K. H. Luo, A critical review on VOCs adsorption by different porous materials: Species, mechanisms and modification methods, *J. Hazard. Mater.*, 2020, **389**, 122102.

40 M. N. Sweety and S. Islam, A Rietveld refinement in WPPF analysis for crystallographic behavior study of nanocrystal anatase TiO_2 synthesized by ultrasonic-assisted sol–gel method and its photocatalytic activity, *J. Cryst. Growth*, 2025, 128424.

41 J. P. Bezzina, L. R. Ruder, R. Dawson and M. D. Ogden, Ion exchange removal of Cu(II), Fe(II), Pb(II), and Zn(II) from acid-extracted sewage sludge–Resin screening in weak acid media, *Water Res.*, 2019, **158**, 257–267.

42 Y. Cheng, H. Li, C. Fang, L. Ai, J. Chen, J. Su, Q. Zhang and Q. Fu, Facile synthesis of reduced graphene oxide/silver nanoparticles composites and their application for detecting heavy metal ions, *J. Alloys Compd.*, 2019, **787**, 683–693.

43 Z. Li, Y. Kong and Y. Ge, Synthesis of porous lignin xanthate resin for Pb^{2+} removal from aqueous solution, *Chem. Eng. J.*, 2015, **270**, 229–234.

44 Z. Wu, W. Huang, X. Shan and Z. Li, Preparation of a porous graphene oxide/alkali lignin aerogel composite and its adsorption properties for methylene blue, *Int. J. Biol. Macromol.*, 2020, **143**, 325–333.

45 X. Gao, C. Guo, J. Hao, Z. Zhao, H. Long and M. Li, Adsorption of heavy metal ions by sodium alginate-based adsorbent: a review and new perspectives, *Int. J. Biol. Macromol.*, 2020, **164**, 4423–4434.

46 H. Che, G. Che, P. Zhou, C. Liu and H. Dong, Yeast-derived carbon sphere as a bridge of charge carriers towards enhanced photocatalytic activity of 2D/2D Cu_2WS_4/g-C_3N_4 heterojunction, *J. Colloid Interface Sci.*, 2019, **546**, 262–275.

47 M. Zhang, L. Song, H. Jiang, S. Li, Y. Shao, J. Yang and J. Li, Biomass-based hydrogel as an adsorbent for the fast removal of heavy metal ions from aqueous solutions, *J. Mater. Chem. A*, 2017, **5**(7), 3434–3446.

48 E. A. Matter, A. F. Hassan, N. M. Elfaramawy and G. Esmail, Enhanced adsorption of lead(II) ions onto cellulose nanoparticles/chitosan composite based on loofah sponge: kinetic and thermodynamic studies, *Biomass Convers. Biorefin.*, 2025, **15**(7), 10961–10976.

49 E. C. Matei, M. A. Rapa, C. I. Covaliu, A. M. Predescu, A. N. Turcanu, C. R. Predescu, D. A. Ignat and G. R. Vlad,

Sodium alginate-cellulose-nano-clay composite adsorbent applied for lead removal from wastewater, *Rev. Chim.*, 2020, **71**(3), 416–424.

50 A. L. Obsa, N. T. Shibeshi, E. Mulugeta and G. A. Workeneh, Eco-friendly composite hydrogel based on cellulose and bentonite for removal of lead(II): Kinetics and isotherm studies, *Carbohydr. Polym. Technol. Appl.*, 2025, **9**, 100637.

51 M. M. Vojkan, J. Milan, Đ. Snežana, S. Maja, S. Staniša, V. Maja and N. Bojanić, The removal of lead(II) ions from aqueous solutions by acid-activated clay modified with sodium carboxymethyl cellulose, *Appl. Ecol. Environ. Res.*, 2017, **15**(4), 1461–1472.

52 A. Alipour, S. Zarrinabadi, A. Azimi and M. Mirzaei, Effective removal of heavy metal using cellulose nanocomposite adsorbents: response surface methodology, *Iran. J. Energy Environ.*, 2022, **13**(3), 258–272.

53 A. Abdolali, H. H. Ngo, W. Guo, J. L. Zhou, J. Zhang, S. Liang and Y. Liu, Application of a breakthrough biosorbent for removing heavy metals from synthetic and real wastewaters in a lab-scale continuous fixed-bed column, *Bioresour. Technol.*, 2017, **229**, 78–87.

54 D. Bulgariu and L. Bulgariu, Sorption of Pb(II) onto a mixture of algae waste biomass and anion exchanger resin in a packed-bed column, *Bioresour. Technol.*, 2013, **129**, 374–380.

55 S. Cheng, Y. Liu, B. Xing, X. Qin, C. Zhang and H. Xia, Lead and cadmium clean removal from wastewater by sustainable biochar derived from poplar saw dust, *J. Cleaner Prod.*, 2021, **314**, 128074.